An Outlook on Potentialities and Limits in Using Epitaxial Polysilicon for MEMS Real-Time Clocks

Giorgio Mussi, Marco Bestetti, Valentina Zega, Attilio Frangi, Gabriele Gattere, and Giacomo Langfelder, *Member, IEEE*

***Abstract*—Epitaxial polysilicon is a cheap material that has been used in the MEMS industry for a long time. Its relatively large -30 ppm/K Temperature Coefficient of frequency (TCf) has prevented its widespread use in real-time clock (RTC) applications. This work investigates the possibility to use this material to build resonators to be used in real-time clock applications, starting from the assumptions that the TCf of polysilicon is large but very repeatable. This would allow a large manufacturer to use a time-saving, thus inexpensive, family compensation, where the calibration procedure is computed for a very small fraction of the population of produced RTCs and then applied to the entire production output. This work presents a novel design of capacitive resonators for RTCs and demonstrates that the spread of the part-to-part temperature dependence is low enough to allow an electronic family compensation to within $\pm$20 ppm of the output frequency.**

***Index Terms*—Clocks, Frequency control, Microelectromechanical systems, Timing.**

I. Introduction

MICROELECTROMECHANICAL system (MEMS) based real time clocks (RTC) have recently become an alternative to quartz-based solutions [1], by narrowing the performance gap on the key requirements. These are essentially represented by a µA-range current consumption, around $10\,\mathrm{ns}$ jitter and 10-100 ppm stability (depending on the target application) for a $32\,\mathrm{kHz}$ RTC output [2], [3].

As silicon and polysilicon have a temperature coefficient of the Young modulus of about $-60\,\mathrm{ppm/K}$ (and of frequency, TCf, which lies in turn in the order of $-30\,\mathrm{ppm/K}$), compensation strategies should be identified to cope with the mentioned stability requirements over e.g. the consumer temperature range ($-40\,^\circ\mathrm{C}$ to $85\,^\circ\mathrm{C}$). These compensation strategies can be of different types, depending on whether the compensation effort is put on the fabrication process, on the electronics, or both. Heavy doping compensation of monocrystalline silicon has proved to be effective in minimizing the TCf [4], [5], and it is currently used in several products. However, this solution still brings a few disadvantages. First, it does not reduce the TCf to a value such that further electronic compensation is not needed; besides, initial offset (i.e. deviation of the resonance frequency at a reference temperature from its desired value), due to unavoidable process spreads (doping and etching), still requires electronic or electromechanical compensation. Mixed-signal analog and digital electronic blocks are used for this purpose [6]. Second, the final TCf depends on the effective doping concentration: best compensation is obtained for very large doping levels (e.g. $1 \times 10^{20}\,\mathrm{cm^{-3}}$), for which however the TCf variation with small doping changes may become non-negligible. Additionally, compensation depends on the crystallographic cut direction of monocrystalline silicon. This introduces further uncertainty on the TCf due to spreads in the crystallographic cut direction. All these uncertainties make part-to-part calibration of the TCf necessary, e.g. with a five-point calibration as in [6]. Third, the use of monocrystalline silicon-on-insulator (SOI) wafers represents a higher cost for manufacturers than polysilicon-based processes, e.g. those already used for mass production of inertial sensors [7]. Although this work is focused on technical aspects, it is correct to present it in the industrial and economical context of these days. Therefore, more details about this point are given in a dedicated Appendix at the end of the paper.

All these considerations suggest investigating the possibility of pure electronic compensation of resonators built in standard epitaxial polysilicon, so to avoid the use of SOI, and to reduce the number of parameters that affect the TCf. While a few works already researched on this topic, even though on piezoelectric resonators [8], [9], the target of this study is to exploit a statistical investigation of the TCf repeatability in an epitaxial polysilicon process with low doping levels, and to verify the possibility of a family compensation of the TCf instead of a part-to-part compensation. In a family compensation, only a few parts (e.g. 10 to 100, named the training set) of the family (e.g. 1000 to 10 000 resonators of a wafer or a lot) are characterized, and their average behavior is used to compensate all parts in the family. This approach consistently reduces the calibration time of products, at the cost of a lower calibration accuracy.

To achieve the targets above, the work develops as follows: Section II introduces and motivates the design of the studied resonator topologies, with varying geometry and operating frequency. Relying on the resonator electromechanical parameters, Section III discusses the design of the electronics used in the following sections and describes the setup. Section IV presents a thorough experimental campaign on about 40 samples of different type (the training set) to accurately

Manuscript received April 4, 2019; revised July 6, 2019; accepted August 18, 2019.

Giorgio Mussi, Marco Bestetti and Giacomo Langfelder are with the Dipartimento di Elettronica, Informazione e Bioingegneria, Politecnico di Milano, Milan, Italy (e-mail: giorgio.mussi@polimi.it).

Valentina Zega and Attilio Frangi are with the Dipartimento di Ingegneria Civile e Ambientale, Politecnico di Milano, Milan, Italy.

Gabriele Gattere is with the Analog and MEMS Group, STMicroelectronics, Cornaredo, Italy.

measure the TCf and to derive a 2nd-order model to describe its temperature behavior. The model is derived starting from spectral-sweep responses in open-loop excitation of the resonator, at different temperature values, with post-processing routines. To demonstrate the possibility of pure electronic compensation, resonators of the family, but not belonging to the training set, are then tested vs temperature in closed-loop mode in Section V, both with discrete and with integrated low-power oscillators. The captured frequency is corrected using the model above, demonstrating a family compensation whose coefficients reliably derive only from the mechanical drift of the resonance frequency found in open-loop, and not from the used electronics. The technique is effective in compensating temperature variations within $\pm 20\,\mathrm{ppm}$, the residual error being comparable to the setup tolerance in terms of temperature measurement. Note that the aim here is not to outperform few-ppm or sub-ppm stability levels obtained in other works with multi-point temperature calibration, but to show that few tens of ppm stability can be achieved with much cheaper wafers and without long and expensive part-to-part temperature calibration procedure. Finally, conclusions and discussions are drawn in Section VI.

II. Resonators Modeling and Design

The capacitive resonators of this work are fabricated with the $24\,\mu\mathrm{m}$ Thick Epitaxial Layer for Micro Accelerometers (ThELMA) process from STMicroelectronics [7]. The structural layer is grown from a standard epitaxy with a N-type doping giving a square resistance of $15\,\Omega/\square$. The process currently delivers more than 1 million capacitive sensors per day, and it would be thus suitable for mass production of low-cost capacitive RTCs. A minimum in-plane gap of $0.8\,\mu\mathrm{m}$ (before over-etch effects) and a maximum resonator footprint of $400\,\mu\mathrm{m} \times 250\,\mu\mathrm{m}$ were chosen by design to cope with a final package footprint of $1\,\mathrm{mm}^2$.

A. Design Considerations: Resonance Frequency

An established technique to achieve an accurate output frequency in a real-time clock relies on a reference based on a resonator with a resonance frequency f_0 much larger than the target frequency f_{out} ($32.768\,\mathrm{kHz}$ usually), and then to apply an integer frequency division by N or $N+1$ with a programmable divider (Fig. 1). The division factor is selected by a compensation machine in such a way that the output frequency matches, on average over a certain number of periods, the target value within the accuracy and stability specifications.

The value of N is determined by the maximum deviations of f_0 from its nominal value. These can be given by process spreads and by temperature changes. The smaller N, the larger the difference Δf between f_0/N and $f_0/(N+1)$, so the larger the range that can be compensated. With a $-30\,\mathrm{ppm/K}$ 1st-order frequency drift, the maximum deviation due to temperature changes in the consumer range ($300\,\mathrm{K}$ $\pm 62\,\mathrm{K}$) turns out to be $\pm 1860\,\mathrm{ppm}$. This is still much lower than process spreads on the frequency, which is dominated by etching non-uniformities and affects similarly polysilicon and SOI devices. This spread can be in the order of $\pm 3\,\%$ ($\pm 30 \times 10^3\,\mathrm{ppm}$). This $\pm 3\,\%$ spread then imposes an upper bound to N, regardless of the TCf of the process, expressed by:

$$\frac{f_0(1+0.03)}{N+1} = \frac{f_0(1-0.03)}{N} \Rightarrow N = 16 \qquad (1)$$

A lower bound is posed by other limitations, because a lower N (i.e. a lower mechanical frequency):

- increases the part-to-part spread on the nominal frequency f_0, due to typically narrower springs.
- increases the effect of the electrostatic softening, due to a lower f_0 hence a typically lower mechanical stiffness.
- decreases the consumption of the sustaining oscillator, due to a lower f_0.
- increases the short-term output frequency variation (i.e. jitter), due to a larger Δf between periods resulting from different division factor.

The programmable division factor N is thus set to 16/17, which implies that the nominal resonator frequency should equal $f_0 = f_{out} \cdot 16.5 = 541\,\mathrm{kHz}$. Note that designing a high-frequency resonator has also the advantages of rejecting acceleration effects on the micromechanical structure (we recall indeed that the displacement induced by an acceleration is proportional to the squared inverse of the resonance frequency).

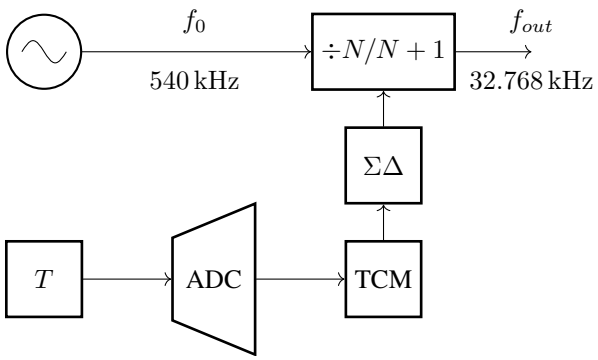

Fig. 1. Block scheme of the compensation system. The reference oscillator produces a periodic signal at frequency f_0. This frequency gets divided by a divider whose division modulus (N or N+1) is selectable. The selection is performed by the temperature acquisition chain, where a temperature sensor T and the subsequent ADC produces a digital word that is elaborated by the temperature compensation machine TCM which controls the modulus of the divider so that the appropriate *average* division factor is achieved. A digital ΣΔ modulator is used to convert the multi-bit information of the ADC/TCM to the single-bit information required by the fractional divider.

B. Design Considerations: Quality Factor and Transduction

Besides the just-discussed frequency stability, the other main system requirement is the power consumption. As for the main oscillator, the consumption is ultimately limited by the equivalent series resistance of the resonator [10]. This parameter is influenced by the resonator quality factor Q and the transduction factor $\eta = V_R \cdot \partial C/\partial x$, V_R being the voltage applied between the resonator rotor (the suspended part) and

This article has been accepted for publication in a future issue of this journal, but has not been fully edited. Content may change prior to final publication. Citation information: DOI 10.1109/TIE.2019.2938465, IEEE Transactions on Industrial Electronics

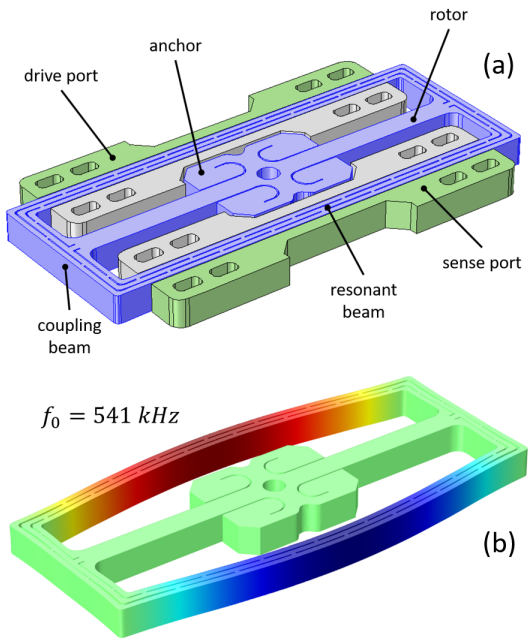

Fig. 2. Computer-aided-design view of the designed resonator (a). Modal shape-function of the flexural mode of the resonator under study (b): drive and sense ports have been hidden for the sake of clarity. The countour of the displacement field is shown in colour.

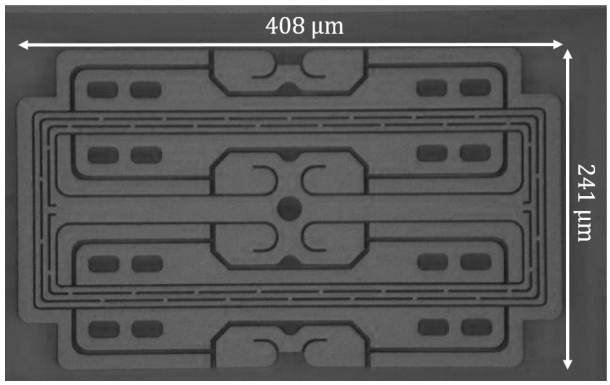

Fig. 3. SEM image of the designed resonator. The actuated slotted beams are 351 µm long and 15 µm wide.

the stators (actuation and sensing port), and $\partial C/\partial x$ being the capacitance variation per unit displacement of the two capacitive ports, assumed nominally identical. To maximize the quality factor, the package pressure was minimized to below $50\,\mu\mathrm{bar}$. A design based on parallel-plate transduction was adopted so to maximize $\partial C/\partial x$ and to add as little mass as possible.

C. Designed Resonators

The considerations above led to the design of the structure presented in Fig. 2a: it is formed by a symmetric scissor-jack architecture with a central anchor region [11]. Under the electrostatic actuation applied at the drive port, the two external beams, anchored through the lateral coupling bars, deflect as shown in Fig. 2b (drive and sense ports not shown for the sake of clarity). All along the suspended part, slots

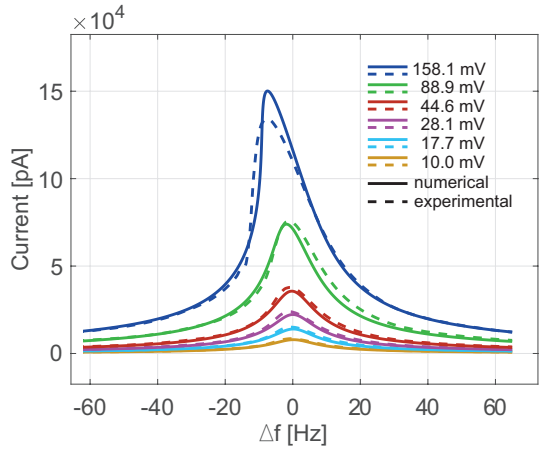

Fig. 4. Frequency response of the MEMS resonator shown in Fig. 2. Experimental curves (dotted lines) are compared to numerical predictions (continuous lines) for different actuation voltages (10 mV, 17.7 mV, 28.1 mV, 44.6 mV, 88.9 mV and 158.1 mV) and for a constant bias voltage of 3.6 V.

are designed to avoid heat flow between points subject to compression and point subject to tension, so to minimize thermoelastic damping contributions [12]. The nominal frequency of the resonator is set by design and through the aid of finite element (FE) simulations to 541 kHz. A scanning electron microscope picture of one resonator is shown in Fig. 3.

In addition to the described structure, three other designs were implemented with slight variations to verify the effectiveness of the slotting and the impact of the anchor losses. This translates into a population of similar device each differing from the rest in terms of quality factor, motional resistance, and nominal resonance frequency. Detailed description of these devices is not given as they are not as optimized as the proposed design: nevertheless, they can be used to increase the training set for the evaluation of the TCf behavior.

D. Non-Linearity Modeling

Large actuation voltages are desirable in an oscillator, in order to decrease phase noise. Additionally, a relatively large voltage amplitude in one point of the oscillator eases the design of the comparator that generates a square-wave clock out of the harmonic oscillating signal. On the other hand, a large actuation voltage can excite non-linear phenomena, both in the mechanical structures and in the electrostatic readout [13]. The larger these non-linear phenomena, the more the resonance frequency shifts away from the nominal small-signal condition and the more complex the system behavior becomes. With the aim of estimating the effect of nonlinearities and to find the linearity boundaries, a series of numerical analyses for the structure of Fig. 2 was performed.

Geometric nonlinearities were simulated through the FEM reduced order model described in [14], which is a force-based indirect method that accounts for the stress redistribution occurring in large transformations. On the other side, nonlinear electrostatic forces have been accounted for through a standard code based on integral equations which follows the actual

deformation of the structure. Thermoelastic damping was estimated using commercial FEM codes yielding a thermoelastic quality factor $Q_{TED} = 50\,000$ for the geometry under study. Finally, a numerical code able to compute the gas damping and the associated quality factor Q_{GAS} was also employed [15], [16]. Due to the length scale and the near vacuum working pressure (nominally equal to $10\,\mu\mathrm{bar}$), the flow develops in the so called free-molecule regime where collisions between molecules can be neglected and simplified and fast simulation tools for the prediction of near vacuum gas damping can be employed [15]. Despite the pressure inside the package is very low, the effect of fluid damping on the overall quality factor cannot be considered negligible, even at very low displacement ranges (i.e. $Q_{TOT} = 42\,567$ for displacements of the beam equal to $26\,\mathrm{nm}$) and increases with the displacement magnitude.

The one degree of freedom nonlinear model obtained by combining the different contributions, simulated separately as explained above, was finally solved through a continuation method with arc length control to simulate both stable and unstable branches. In Fig. 4, the numerical predictions, computed assuming the nominal $10\,\mu\mathrm{bar}$ pressure in the package, are reported together with the experimental frequency responses of the resonator for different driving voltages and for a DC bias voltage of $3.6\,\mathrm{V}$. A good agreement is found despite numerical predictions are computed by considering nominal geometric dimensions of the device and material parameters taken from the literature. In the end, an AC drive voltage of $80\,\mathrm{mV}$ at most will be used in the following sections to test the fabricated devices. Note that, in general, operating an oscillator in the mechanical nonlinear regime is not necessarily forbidden, but, as the main goal of this work is to study the thermal drift mechanism and its repeatability, it is better to isolate as much as possible this phenomenon from other possible overlapping phenomena.

III. Measurement Setup

As for the experimental part of this work, two different electronic systems were developed. The first one is a discrete-component versatile board that is initially used as an open-loop chain to purely characterize the temperature behavior of the resonators transfer function. Through this board, the training set data are generated and the temperature compensation model is defined. The same board can be switched to a closed-loop mode feedback oscillator, which can be used to assess the model validity on samples different from the training set, thus implementing a family compensation. The second electronic system is a low-power integrated Pierce oscillator. Its purpose is again to assess the validity of the family compensation, this time coping also with noise and consumption requirements. The two systems are described in the following subsections. When operating in closed-loop, they both provide a maximum driving voltage lower than $80\,\mathrm{mV}$, to excite the resonator in its linear regime, according to the results discussed in Fig. 4.

A. Characterization with PCB in Open Loop

To perform an extensive characterization of the TCf on the sample population, the board whose schematic is shown in Fig. 5 was used in the open-loop configuration. The resonators are coupled to the board using a CLCC68 carrier and bonding wires. A drive signal is injected into the drive port by a network analyzer; the motional current at the resonator output is readout by a charge amplifier stage (nominally with $500\,\mathrm{fF}$ feedback capacitance, $1\,\mathrm{G\Omega}$ feedback resistance), further amplified and sent back to the network analyzer input so to measure the input/output transfer function (stages indicated by dashed lines are disconnected in this operation mode). An initial careful calibration of the charge amplifier gain (which

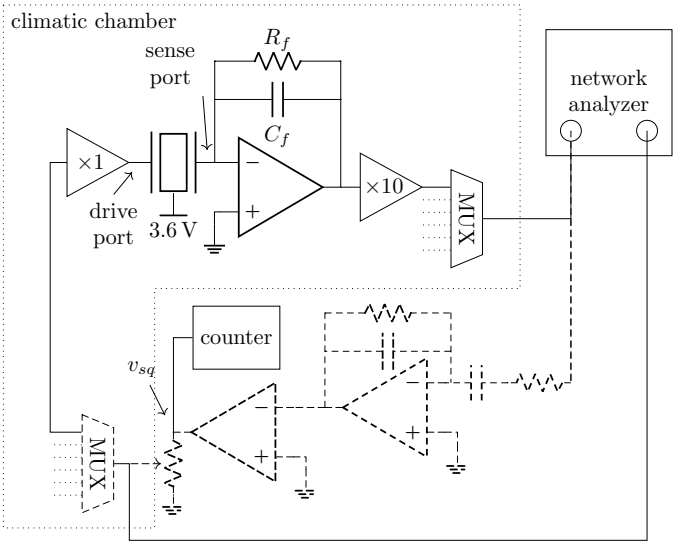

Fig. 5. Sketch of the setup used to characterize the main electromechanical parameters, namely the motional resistance R_m, the quality factor, the transduction factor and the linearity. The dashed portion of the schematic is used (with a proper configuration of switches not shown) to close the loop around the resonator forming an oscillator for closed-loop measurements.

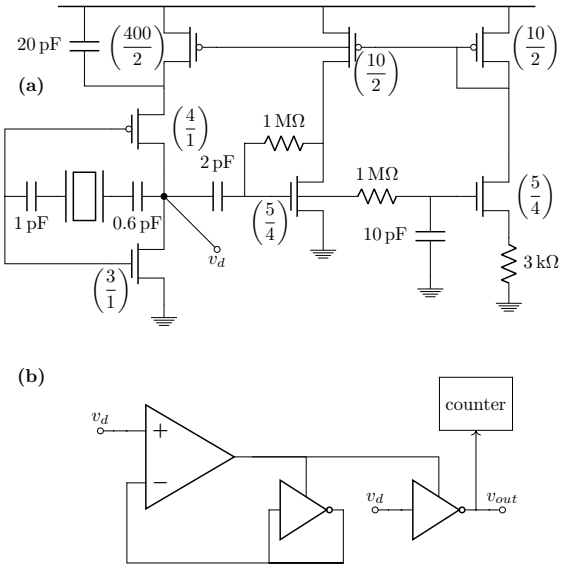

Fig. 6. (a) Schematic of the implemented integrated Pierce oscillator with its AGC loop. The architecture is based on the work in [17] and adapted to the discussed resonator design. (b) Schematic of the comparator circuit. The two identical inverters have a transistor in series to starve the bias current and reduce the consumption.

depends on the nominal feedback impedance of the charge amplifier and on the parasitics in parallel to it) is performed by computing the gain of each chain with fixed calibrated capacitors in place of the MEMS resonator.

Using an analytical fitting to the experimental data as detailed e.g. in [18], it is possible to extract the resonator motional resistance, resonance frequency and quality factor. These parameters (with a particular focus on the resonance frequency, for this work) can be evaluated as a function of temperature, by putting the board inside a climatic chamber. Temperature is controlled by a sensor positioned close to the MEMS resonators die, with a resolution of $0.15\,\mathrm{K}$. The resonator linearity can also be tested as a function of the driving amplitude set through the network analyzer. The board actually includes four driving/sensing front-end stages, so to parallelize the measurements on the four different structures of a single die.

B. Characterization with PCB in Closed Loop

The same board can be used in closed-loop mode. In this case, the output of the charge amplifier is sent to a 90 degree shifter (to cope with Barkhausen conditions), squared by a high-gain stage (to provide the necessary nonlinearity in the oscillation loop [19], [20]), and de-amplified down to 50 mV (to drive the MEMS in its linear region, according to Fig. 4), before entering the driving port and self-sustain the resonator oscillation. These additional blocks are indicated with dashed lines in Fig. 5. All the singularities of the circuit were placed at least two decades away from resonance, so to avoid undesired phase shifts and oscillation occurring not at the resonant peak.

When the board is switched on, noise components at resonance begin to be amplified until the high-gain stage clamps the oscillation and automatically sets the loop gain to unity. The oscillating frequency in closed-loop mode is measured by a frequency meter, connected to the square wave signal indicated as v_{out} in the figure.

C. Low-Power Integrated Oscillator

In ultra-low-power applications, unwanted temperature dependencies may arise from the electronics side, and in particular from the oscillator. It is therefore interesting to perform the previous experiment in a system where consumption constraints are also taken into account.

To this aim, the low-power oscillator shown in Fig. 6a, integrated in a $0.35\,\mu\mathrm{m}$ process, was designed and tested with the resonators. The oscillator implements a Pierce topology, with a complementary transconductor. Supposing that the transistors are operated in the sub-threshold region for maximum efficiency, the minimum current consumption I_{min} of this configuration is given by:

$$I_{min} = \frac{1}{2}\omega_0^2 C_1 C_2 R_m n V_{th}, \tag{2}$$

where C_1 and C_2 are the capacitors in parallel to the resonator drive/sense electrodes, n is the sub-threshold slope of the MOS transistor, V_{th} the thermal voltage [17] and the factor $1/2$ is due to the complementary transconductor.

The bias current of the oscillator is controlled by an automatic gain control (AGC) loop. Thus, no more current than the bare-minimum needed to sustain the oscillation is drawn from the supply, apart from a small overhead due to the AGC itself. Conversely, the sinusoidal oscillation amplitude is relatively small (about $100\,\mathrm{mV}$) and so the comparator that creates the squarewave reference for the system must be designed with a threshold reliably set near the middle of the sinusoidal oscillation. In this work, the comparator is implemented with a novel architecture as in Fig. 6b: an inverter whose threshold V_{TH} is matched to the DC level of the oscillating voltage v_d. To achieve this, a replica inverter has its input and output nodes shorted together, so that their potential is exactly V_{TH}, and draws the supply voltage from the output of an OTA. The loop, if designed with sufficient low-frequency loop gain, matches the threshold of the replica inverter with the DC level of v_d. The AC component of v_d is ignored due to the very limited bandwidth of the loop. The output of the OTA supplies also the inverter that effectively acts as a comparator, so that the threshold voltage is properly set and the output v_{out} correctly switches.

IV. Characterization vs Temperature

To characterize the f_0 drift in temperature, the setup described in Section III-A is placed inside a climatic chamber. The temperature is varied from $5\,^\circ\mathrm{C}$ to $85\,^\circ\mathrm{C}$ in $10\,^\circ\mathrm{C}$ steps. Sub-$0\,^\circ\mathrm{C}$ temperatures were avoided to prevent water vapor condensation on exposed bonding wires and because of some instability in the chamber controller loop at $5\,^\circ\mathrm{C}$ and below. Each measurement (as described in Section III-A) is performed twenty minutes after the temperature monitored by the sensor reaches the target value. The uncertainty in the frequency-vs-temperature measurements is dominated by the $0.15\,\mathrm{K}$ resolution of the temperature sensor, which translates into a $\pm 3\,\sigma$ uncertainty on the measured resonance frequency of about $\pm 14\,\mathrm{ppm}$ [18].

The following polynomial law is used in this work to describe the TCf of the resonators:

$$\Delta f_{ppm}(T) = TCf_1 \cdot (T - T_0) + TCf_2 \cdot (T - T_0)^2. \tag{3}$$

and one of the goals of this characterization is to extract the values for the coefficients TCf_1 and TCf_2.

The measured frequency-vs-temperature characteristics were extracted for 11 dies, each containing the 4 aforementioned structures: the results are shown in Fig. 7a. The observed spread in the native frequency (within $\pm 3000\,\mathrm{ppm}$) at a given temperature is well predicted by anaytical models if a process etching spread of $\pm 0.15\,\mu\mathrm{m}$ is considered, which affects the beam width and mass. The spread is thus not dependent on the specific epitaxial process used in this work, but on the etching equipment. The trends show a maximum spread in the ambient-temperature f_0 of the resonators of about $0.5\,\%$ and a roughly linear temperature drift. This proves that the linear TCf is the dominant drift contribution for the used epitaxial polysilicon. From each of these curves the best fitting line was extracted, with an average value across the 4 different designs of $-30.9\,\mathrm{ppm}/^\circ\mathrm{C}$.

This article has been accepted for publication in a future issue of this journal, but has not been fully edited. Content may change prior to final publication. Citation information: DOI 10.1109/TIE.2019.2938465, IEEE Transactions on Industrial Electronics

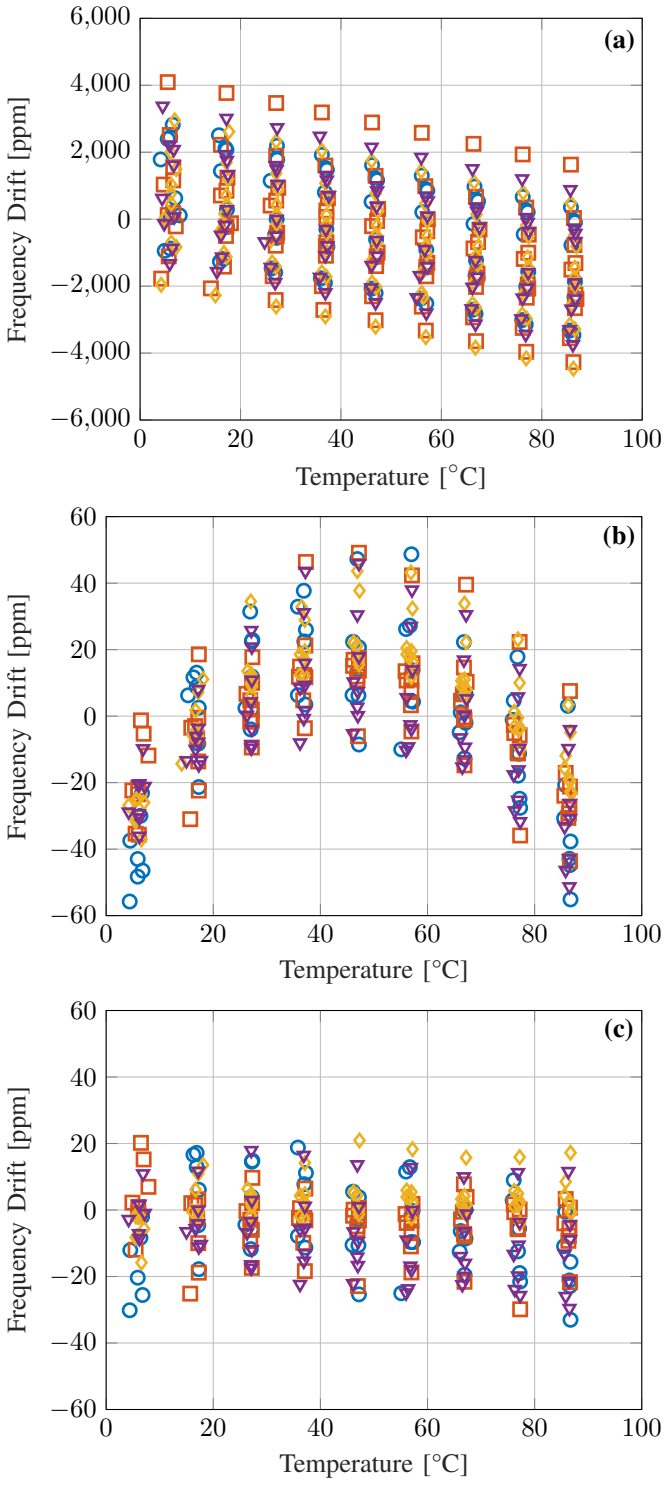

Fig. 7. (a) Measured resonance frequencies of the training samples. The frequency offset due to process variation is larger than the total drift across the temperature range by a factor of 3. (b) Frequency drift after a 1st-order compensation of the TCf. This (and the following) residual plot is obtained by applying to each individual sample the *average* fitting. (c) Frequency drift after a 2nd-order compensation of the TCf. The final limit of $\pm 20\,\mathrm{ppm}$ is believed to be caused by imperfections in the temperature measurement.

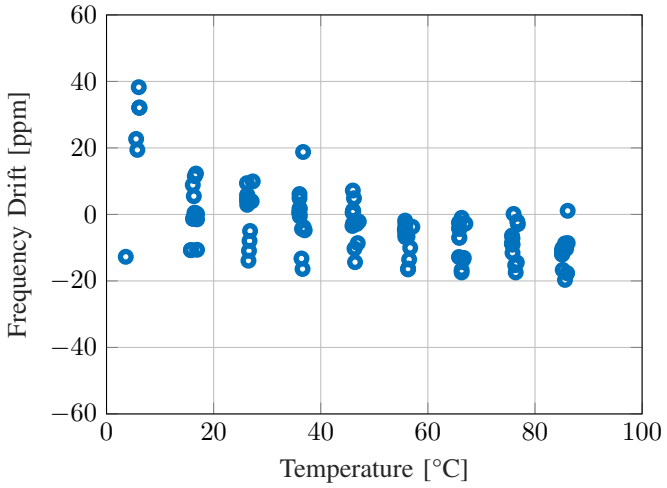

Fig. 8. Verification dataset from PCB oscillator. The residual frequency drift is bounded at ± 20 ppm. None of these samples were used to compute the average compensating polynomial. The larger frequency drift at the lower end of the temperature range is due to a larger uncertainty in the actual MEMS temperature in a slightly more unstable environment.

A. 1st-order Compensation

To investigate the feasibility of a family compensation of such resonators, the frequency-vs-temperature drift data were compensated mathematically by subtracting the average slope (1st-order compensation). The average was computed across all devices, without discriminating the different designs with the aim of exposing the proposed technique to a possibly-increased variability. The frequency offset at room temperature was instead subtracted on a device-by-device basis, mimicking a one-point calibration for each device. The result of this procedure is shown in Fig. 7b, where the 1st-order residuals of each sample of each design are plotted against temperature. The obtained result shows a maximum $\pm 60\,\mathrm{ppm}$ frequency error across the sample population after the family compensation. This error is already compatible with the low-end of RTC applications and is dominated by a fairly repeatable 2nd-order Frequency Temperature Coefficient (TCf_2) of $-24\,\mathrm{ppb/°C^2}$.

B. 2nd-order Compensation

The repeatability of the TCf_2 is qualitatively evident from Fig. 7b, so that one can apply the family-compensation technique accounting for the TCf_2 as well. The result of this procedure is shown in Fig. 7c. No higher-order trend is highlighted and a residual drift of about $\pm 20\,\mathrm{ppm}$ is reached. This limit is compatible with the estimation of the measurement error on the frequency samples due to the setup limitations (in particular, the accuracy of the temperature sensor), which hints at the possibility that the part-to-part spread in temperature is even smaller than the observations of the experiment.

The model described by Eq. 3, resulting from the measured training set, thus becomes:

$$\Delta f_0(T) = 28.64 \times (T - T_0) - 0.024 \times (T - T_0)^2 \quad [\mathrm{ppm}]$$

This article has been accepted for publication in a future issue of this journal, but has not been fully edited. Content may change prior to final publication. Citation information: DOI 10.1109/TIE.2019.2938465, IEEE Transactions on Industrial Electronics

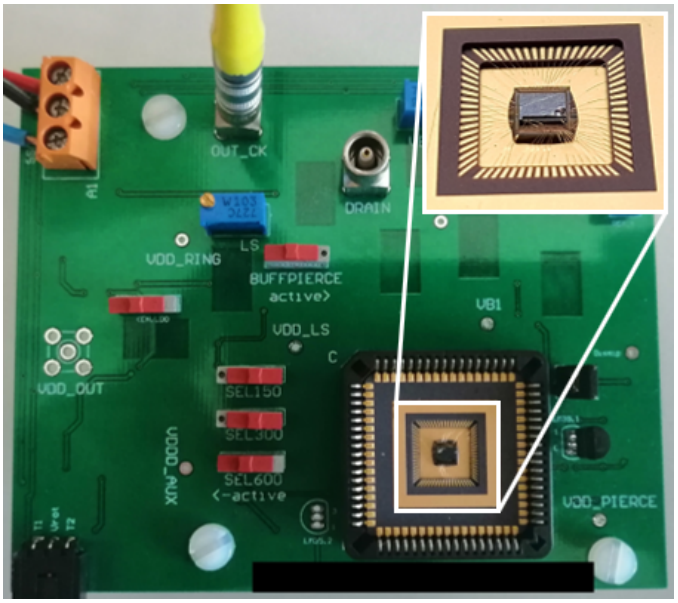

Fig. 9. Picture of the test board used for the characterization of the integrated oscillator. The oscillator and the MEMS dies are connected together and to the ceramic carrier by means of wire-bondings.

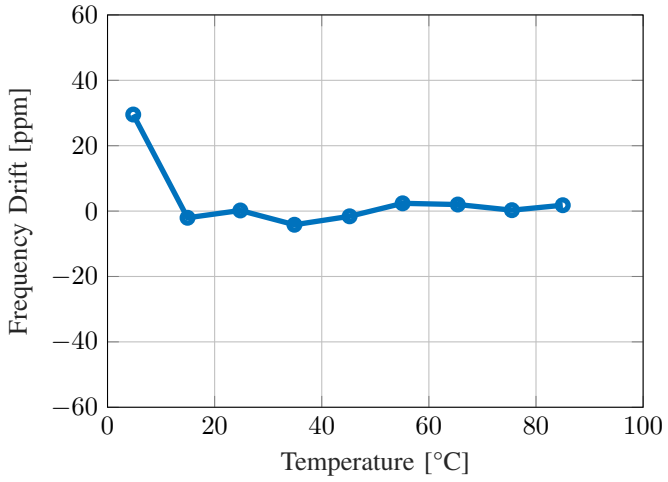

Fig. 10. Result of the 2nd-order compensation applied to the frequency drift measured with a frequency-meter at the output of an integrated Pierce oscillator coupled to the considered resonator.

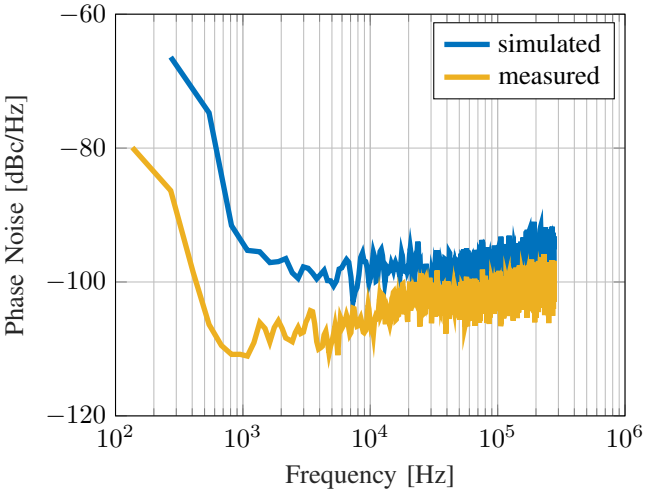

Fig. 11. Phase spectrum at the squarewave output of the oscillator: experimental and simulated data.

V. Validation Measurements

A validation of the presented results was then carried out. This consisted in the application of the calibration technique computed with the measurements presented in Section IV to another set of data not used for the characterization phase (i.e. a verification dataset). Specifically, the verification dataset was taken with a different methodology: the resonance frequencies were not computed as the peak frequency of the resonator transfer function, rather as the oscillating frequency of the closed-loop oscillator, implemented on the PCB or the integrated Pierce.

The purpose of this strategy is to put the system in conditions as close as possible to those of the final application.

A. Validation with PCB Oscillator

The setup described in Section III-B was placed inside the climatic chamber and the oscillation frequencies and temperature were logged for 13 additional resonator samples, not used in the characterization phase and randomly chosen from the same lot. Subsequently, the same compensating polynomial was directly used to compensate this new dataset. The result is shown in Fig. 8.

The residual frequency error stays within $\pm 20\,\mathrm{ppm}$, where no other significant trend or correlation is observed, a result very similar to what was obtained previously on the training dataset. A couple of points deviate from this range at 5° due to the mentioned difficulty in stabilizing temperature, and thus in knowing accurately the resonator temperature (and not just the one given by the temperature sensor).

B. Validation with Integrated Oscillator

The same experiment was performed with the integrated low-power oscillator. A test PCB was designed to test the system composed by the integrated oscillator and the MEMS resonator wire-bonded on a ceramic LCC carrier plugged into an on-board socket. The oscillator draws $1.5\,\mu\mathrm{A}$ from a $3\,\mathrm{V}$ supply. A picture of the setup is shown in Fig. 9.

The result obtained from the experiment is shown in Fig. 10. The result, once again, further validates the statements of this work even at low power consumption as in the future final application. The oscillator does not add significant phase delay so that the frequency of oscillation is shifted from the MEMS resonance and the drift properties are thus not changed.

An additional noise characterization is done to validate predictions. The output frequency was acquired with a counter (Keysight 53230A) for $90\,\mathrm{ms}$ (50 000 samples) and accumulated after removing the bias term. The resulting spectrum is shown in Fig. 11 together with a simulator prediction obtained with the same technique. A slight mismatch between the curves arises because of an imperfect a-priori knowledge of the parasitic capacitances in parallel to the MEMS terminals. This

causes a discrepancy between the real and simulated power consumptions and, therefore, between the noise in the two cases. The overall integrated phase noise results in a jitter of $2\,\mathrm{ns}$, compatible with the target applications.

VI. Conclusion

The present work shows a novel design of MEMS resonators realized in a standard industrial-grade polysilicon epitaxial process for RTC applications and an analysis on their frequency stability across the $5\,^{\circ}\mathrm{C}$ to $85\,^{\circ}\mathrm{C}$ range. The initial hypothesis, that a family compensation (i.e. only a fraction of the produced devices are used for calibration of the $-30\,\mathrm{ppm/K}$ TCf) is theoretically enough to reach a satisfactory stability within the few $10\,\mathrm{ppm}$ to $100\,\mathrm{ppm}$ range, is verified through a measurement campaign. This work represents a fundamental step towards the actual realization of RTCs with a mechanical resonator based on a low-cost industrial poly-silicon process. The presented low-power oscillator will be integrated with a temperature-compensating machine that implements the family compensation identified in this work.

Appendix

In this short Appendix more details are given regarding the difference in terms of cost between the use of an epitaxial polysilicon process versus a heavily-doped silicon-on-insulator process. The former has been used for decades by several MEMS companies for mass production, e.g. in the field of inertial sensors. SOI processes at very high doping levels have been proposed more recently as an advanced technology for the stabilization of the TCf of micromechanical resonators.

The first important difference to note is the cost of the bare wafer. These days, a polysilicon wafer costs approximately \$30, whereas an SOI wafer costs about ten times more ($\approx$\$300). These numbers are well-known to the insiders of the field.

Secondly, obtaining a native $\pm 100\,\mathrm{ppm}$ resonator stability requires doping levels in the order of $1 \times 10^{20}\,\mathrm{cm}^{-3}$ [5], which, to the authors knowledge, are not available off-the-shelf. Thus, a company inevitably needs to buy a thin SOI wafer and to grow themselves the highly-doped crystalline silicon on top of it: this procedure requires to perform several times (e.g. 4-5 cycles for a $20\,\mu\mathrm{m}$ thickness) two steps of (i) dopant implantation and (ii) diffusion plus silicon growth. This procedure involves more process steps and becomes slower than a standard polysilicon epitaxy growth, thus further increasing the process cost.

These considerations, relevant for the industrial electronics community, are at the basis of the technical research proposed in this manuscript.

References

[1] J. Van Beek and R. Puers, "A review of MEMS oscillators for frequency reference and timing applications," *Journal of Micromechanics and Microengineering*, vol. 22, no. 1, p. 013001, 2011.

[2] SiTime, "SiTime 1532 datasheet." [Online]. Available: https://www.sitime.com/datasheet/SiT1532

[3] STMicroelectronics, "M41T62 datasheet." [Online]. Available: https://www.st.com/resource/en/datasheet/m41t62.pdf

[4] T. Pensala, A. Jaakkola, M. Prunnila, and J. Dekker, "Temperature compensation of silicon MEMS resonators by heavy doping," in *Proc. IEEE Int. Ultrasonics Symp*, DOI 10.1109/ULTSYM.2011.0486, pp. 1952–1955, Oct. 2011.

[5] E. J. Ng, C. H. Ahn, Y. Yang, V. A. Hong, C.-. Chiang, E. Ahadi, M. W. Ward, and T. W. Kenny, "Localized, degenerately doped epitaxial silicon for temperature compensation of resonant MEMS systems," in *2013 Transducers Eurosensors XXVII: The 17th International Conference on Solid-State Sensors, Actuators and Microsystems (TRANSDUCERS EUROSENSORS XXVII)*, DOI 10.1109/Transducers.2013.6627294, pp. 2419–2422, Jun. 2013.

[6] S. Zaliasl, J. C. Salvia, G. C. Hill, L. . Chen, K. Joo, R. Palwai, N. Arumugam, M. Phadke, S. Mukherjee, H. Lee, C. Grosjean, P. M. Hagelin, S. Pamarti, T. S. Fiez, K. A. A. Makinwa, A. Partridge, and V. Menon, "A 3 ppm 1.5 $\times$ 0.8 mm 2 1.0 μa 32.768 kHz MEMS-based oscillator," *IEEE Journal of Solid-State Circuits*, vol. 50, DOI 10.1109/JSSC.2014.2360377, no. 1, pp. 291–302, Jan. 2015.

[7] G. Langfelder, S. Dellea, F. Zaraga, D. Cucchi, and M. Azpeitia Urquia, "The dependence of fatigue in microelectromechanical systems on the environment and the industrial packaging," *IEEE Transactions on Industrial Electronics*, vol. 59, DOI 10.1109/TIE.2011.2151824, no. 12, pp. 4938–4948, Dec. 2012.

[8] D. Ruffieux, F. Krummenacher, A. Pezous, and G. Spinola-Durante, "Silicon resonator based 3.2μW real time clock with$\pm$10 ppm frequency accuracy," *IEEE Journal of Solid-State Circuits*, vol. 45, DOI 10.1109/JSSC.2009.2034434, no. 1, pp. 224–234, Jan. 2010.

[9] D. Ruffieux, N. Scolari, F. Giroud, T. Le, S. Dalla Piazza, F. Staub, K. Zoschke, C. Manier, H. Oppermann, T. Suni, J. Dekker, and G. Allegato, "A versatile timing microsystem based on wafer-level packaged XTAL/BAW resonators with sub-μW RTC mode and programmable HF clocks," *IEEE Journal of Solid-State Circuits*, vol. 49, DOI 10.1109/JSSC.2013.2282111, no. 1, pp. 212–222, Jan. 2014.

[10] C. T.-. Nguyen and R. T. Howe, "An integrated CMOS micromechanical resonator high-Q oscillator," *IEEE Journal of Solid-State Circuits*, vol. 34, DOI 10.1109/4.753677, no. 4, pp. 440–455, Apr. 1999.

[11] G. Gattere, A. Tocchio, and C. Valzasina, "Microelectromechanical resonator with improved electrical features," European Patent EP 3 407 492 A1, 2018.

[12] A. Duwel, R. N. Candler, T. W. Kenny, and M. Varghese, "Engineering MEMS resonators with low thermoelastic damping," *Journal of Microelectromechanical Systems*, vol. 15, DOI 10.1109/JMEMS.2006.883573, no. 6, pp. 1437–1445, Dec. 2006.

[13] M. Pardo, L. Sorenson, and F. Ayazi, "An empirical phase-noise model for MEMS oscillators operating in nonlinear regime," *IEEE Transactions on Circuits and Systems I: Regular Papers*, vol. 59, DOI 10.1109/TCSI.2012.2195129, no. 5, pp. 979–988, May. 2012.

[14] A. Frangi and A. Guerrieri, "Modelling geometrical nonlinearities in MEMS resonators," in *First International Nonlinear Dynamics Conference (Nodycon)*, 2019.

[15] P. Fedeli, A. Frangi, G. Laghi, G. Langfelder, and G. Gattere, "Near vacuum gas damping in MEMS: Simplified modeling," *Journal of Microelectromechanical Systems*, vol. 26, DOI 10.1109/JMEMS.2017.2686650, no. 3, pp. 632–642, Jun. 2017.

[16] A. Frangi, P. Fedeli, G. Laghi, G. Langfelder, and G. Gattere, "Near vacuum gas damping in MEMS: Numerical modeling and experimental validation," *Journal of Microelectromechanical Systems*, vol. 25, DOI 10.1109/JMEMS.2016.2584699, no. 5, pp. 890–899, Oct. 2016.

[17] E. A. Vittoz, M. G. Degrauwe, and S. Bitz, "High-performance crystal oscillator circuits: Theory and application," *IEEE Journal of Solid-State Circuits*, vol. 23, no. 3, pp. 774–783, 1988.

[18] G. Mussi, M. Bestetti, V. Zega, A. Frangi, G. Gattere, and G. Langfelder, "Resonators for real-time clocks based on epitaxial polysilicon process: A feasibility study on system-level compensation of temperature drifts," in *Proc. IEEE Micro Electro Mechanical Systems (MEMS)*, DOI 10.1109/MEMSYS.2018.8346654, pp. 711–714, Jan. 2018.

[19] C. Samori, A. L. Lacaita, F. Villa, and F. Zappa, "Spectrum folding and phase noise in lc tuned oscillators," *IEEE Transactions on Circuits and Systems II: Analog and Digital Signal Processing*, vol. 45, DOI 10.1109/82.700925, no. 7, pp. 781–790, Jul. 1998.

[20] G. Langfelder, A. Caspani, and A. Tocchio, "Design criteria of low-power oscillators for consumer-grade mems resonant sensors," *IEEE Transactions on Industrial Electronics*, vol. 61, DOI 10.1109/TIE.2013.2247233, no. 1, pp. 567–574, Jan. 2014.

Giorgio Mussi received the B.Sc. and M.Sc. degrees in Electronics Engineering from Politecnico di Milano, Italy, in 2014 and 2016, respectively. He is currently pursuing the Ph.D. degree in Information Technology with the Dipartimento di Elettronica, Informazione e Bioingegneria at Politecnico di Milano, where he is also a Teaching Assistant. He has authored 7 international publications and has applied for 1 patent. His research interest is focused on low-power analog/mixed-signal integrated electronics for MEMS applications, such as timing and inertial sensors.

Marco Bestetti received the BS and MS degrees in Electronics Engineering from Politecnico di Milano, Italy, in 2015 and 2017, with a MS thesis on MEMS based real-time clocks. He is currently working toward the Ph.D. in Information Technology with the Dipartimento di Elettronica, Informazione e Bioingegneria, Politecnico di Milano. His research includes MEMS and integrated electronics, in particular on low-power FM systems.

Valentina Zega received the B.Sc. and M.Sc. degrees in mathematical engineering from Politecnico di Milano, Milano, Italy, in 2010 and 2013, respectively, and the Ph.D. degree in structural, seismic and geotechnical engineering from Politecnico di Milano in 2017. From 2017 to 2018, she was Post-Doc researcher at Politecnico di Milano and at TU/Eindhoven and is currently an Assistant Professor with the department of civil and environmental engineering, Politecnico di Milano. She is author of 24 papers and of two deposited patents. Her research interests include the mechanical design and optimization of MEMS devices and metamaterials and the numerical modelling of their nonlinear dynamic response.

Attilio A. Frangi received the M.Sc. degree in aeronautical engineering and the Ph.D. degree in structural engineering from the Politecnico di Milano, Italy, in 1994 and 1998, respectively. From 2001 to 2014, he was an Associate Professor with the Department of Mechanics, École Polytechnique, France. He is currently a Full Professor with the Department of Civil and Environmental Engineering, Politecnico di Milano. He has authored over 150 publications on themes of computational mechanics with a special focus on the simulation of multiphysics phenomena for microsystems.

Gabriele Gattere received the B.Sc. and M.Sc. degrees in mechanical engineering from the Politecnico di Milano, Italy, in 2011 and 2013. During 2013 he was a Visiting Fellow at the Warwick manufacturing group, Warwick University (UK), working on process monitoring for remote laser welding. Since 2014, he has been working with STMicroelectronics in the MEMS design team, currently covering the position of Senior MEMS Designer. His focus is on capacitive and piezoelectric MEMS for sensor and timing applications. He is author and co-author of more than 10 scientific publications in international journals and conference proceedings. He has filed for several patents. In 2014 he was a recipient of the F. Soavi Prize from the Italian Association of Mechanical Technology.

Giacomo Langfelder received the Ph.D. in Information Technology in 2009 from the Politecnico di Milano, Italy, where he is an Associate Professor of MEMS and Microsensors. He is the author of more than 110 publications and applied for more than 10 patents. His research focuses on sensors and related electronics. Dr. Langfelder has been a member of the TPC of various IEEE conferences since 2016. He was a recipient of the Accenture prize in 2005 and the Rotary International prize in 2011.